

Spin-flip Raman scattering of the Γ - X mixed exciton in indirect band gap (In,Al)As/AlAs quantum dots

J. Debus,^{1,*} T. S. Shamirzaev,^{2,3} D. Dunker,¹ V. F. Sapega,^{4,5} E. L. Ivchenko,⁴ D. R. Yakovlev,^{1,4}
A. I. Toropov,² and M. Bayer^{1,4}

¹*Experimentelle Physik 2, Technische Universität Dortmund, 44227 Dortmund, Germany*

²*Rzhanov Institute of Semiconductor Physics, Siberian Branch of Russian Academy of Sciences, 630090 Novosibirsk, Russia*

³*Ural Federal University, 620002 Ekaterinburg, Russia*

⁴*Ioffe Physical-Technical Institute, Russian Academy of Sciences, 194021 St. Petersburg, Russia*

⁵*Spin Optics Laboratory, St. Petersburg State University, 198504 St. Petersburg, Russia*

(Received 26 February 2014; revised manuscript received 2 September 2014; published 19 September 2014)

The band structure of type-I (In,Al)As/AlAs quantum dots with band gap energy exceeding 1.63 eV is indirect in momentum space, leading to long-lived exciton states with potential applications in quantum information. Optical access to these excitons is provided by mixing of the Γ - and X -conduction-band valleys, for which their spins may be oriented by resonant spin-flip Raman scattering. This access is used to study the exciton spin-level structure by accurately measuring the anisotropic hole and isotropic electron g factors. The spin-flip mechanisms for the indirect exciton and its constituents as well as the underlying optical selection rules are determined. The spin-flip intensity is a reliable measure of the strength of Γ - X -valley mixing, as evidenced by both experiment and theory.

DOI: [10.1103/PhysRevB.90.125431](https://doi.org/10.1103/PhysRevB.90.125431)

PACS number(s): 78.67.Hc, 73.21.La, 78.30.Fs, 85.75.—d

I. INTRODUCTION

While semiconductor quantum dots (QDs) have been established as efficient light emitters and detectors in optoelectronics [1], other applications are only prospective so far. Particular examples are implementations in spin electronics and quantum information technologies. For these purposes, the QDs are typically loaded with resident carriers whose spins are well protected from relaxation by the three-dimensional confinement [2,3]. In this context, exciton complexes are often used for spin manipulation [4,5], but are considered less promising as information carriers. This reservation is primarily related to the limited exciton lifetime of about a nanosecond [6], which is too short to provide sufficient coherent manipulation [7]. This situation may change if the exciton lifetime could be extended significantly.

Interesting but technologically challenging in this respect is the placement of QDs in photonic crystals, in which their radiative decay could be suppressed [8,9]. As an alternative to the bright excitons, dark excitons with lifetimes in the μ s range may be used as information carriers; this, however, complicates the direct optical manipulation, but manipulation through the biexciton state can be realized instead [10]. Another possibility is the realization of QDs with a band gap that is indirect in real or momentum space. Here, we focus on self-assembled (In,Al)As/AlAs QDs, in which a crossover of the lowest conduction-band states between the Γ and X valley occurs [11], depending on the dot size. This crossover is reflected by the lifetime of the corresponding exciton, which is formed by a Γ -valley heavy hole and a Γ - or an X -valley electron. Both carriers are spatially located within the QD (type-I band alignment). Due to the valley mixing in the conduction band, the lifetime of that exciton can be as long as

hundreds of μ s [12], which may allow sufficient manipulation within this time span.

The study and manipulation of an X -valley electron and, in turn, an exciton that is indirect in momentum space by optical techniques poses, in general, a significant problem: the associated optical transitions are forbidden in bulk crystals and are only weakly allowed in QDs due to breaking of the translational symmetry. This limitation may be bypassed by utilizing the state mixing of the direct and indirect conduction-band minima in the (In,Al)As/AlAs QDs. One appealing optical technique, i.e., resonant spin-flip Raman scattering (SFRS), may then allow one to study the spin properties of the indirect exciton. SFRS spectroscopy, however, is not only a powerful tool to probe spins by measuring g factors, but is also able to exploit spin interactions to orient spins. It has been successfully applied to quantum wells [13,14] and nanocrystals [15], and has been suggested for direct-gap QD studies [16].

In this paper, we demonstrate that excitons that are indirect in momentum space can be addressed optically by SFRS in an ensemble of undoped (In,Al)As/AlAs QDs. We use SFRS to characterize the Γ - X -valley electron state mixing. It provides access to the fine structure of the indirect exciton and allows us to measure the g -factor tensor components of the indirect exciton and its constituents. The resonant SFRS further enables the preparation of their spin states as well as the determination of the spin-flip mechanisms and optical selection rules. The electron spin-flip energy and efficiency are theoretically modeled by considering an acoustic phonon scattering process including the exciton lifetimes and Γ - X -mixing parameters.

The studied structure contains 20 layers of undoped (In,Al)As/AlAs QDs grown by molecular-beam epitaxy on a (001)-oriented GaAs substrate. The density of the lens-shaped QDs with an average diameter of 15 nm and height of 4 nm is about $3 \times 10^{10} \text{ cm}^{-2}$ in each layer. The QD layers are separated from each other by 20-nm-thick AlAs barriers, which prevent

*Corresponding author: joerg.debus@tu-dortmund.de

an electronic coupling between QDs in adjacent layers. For the SFRS measurements, the sample is mounted strain free on a rotatable stage. It is immersed in pumped liquid helium at a temperature of $T = 1.8$ K and subjected to magnetic fields up to $B = 10$ T. The scattered light is analyzed by a 1-m focal-length double monochromator equipped with a cooled GaAs photomultiplier providing a spectral resolution of about $10 \mu\text{eV}$. For excitation, a tunable continuous-wave Ti:sapphire laser is used with a power density at the sample of $P \leq 15 \text{ W/cm}^2$. The SFRS spectra are measured in the backscattering geometry with circular or linear polarization for the incident and scattered light [14]. The angle θ between the magnetic field \mathbf{B} and the QD growth axis \mathbf{z} is varied between 0° (Faraday geometry) and 90° (Voigt geometry).

II. PHOTOLUMINESCENCE OF DIRECT AND INDIRECT BAND GAP QUANTUM DOTS

Dispersion in dot size, shape, and composition within the ensemble leads to formation of (In,Al)As/AlAs QDs with different band alignments, as shown in Fig. 1(a). The electron (e) ground state changes from the Γ to the X valley with decreasing dot diameter, while the heavy-hole (hh) ground state remains at the Γ point. This corresponds to a change from a direct to an indirect band gap in momentum space while type-I band alignment is preserved [11,17]: the lowest electron level arises from the X valley in small-diameter QDs with strong quantum confinement along the growth direction. With increasing dot diameter, the Γ -valley level shifts to lower energies more rapidly than the X level, due to the smaller effective mass of Γ -valley electrons [18]. For a particular dot diameter, the Γ - and X -electron levels intersect. The

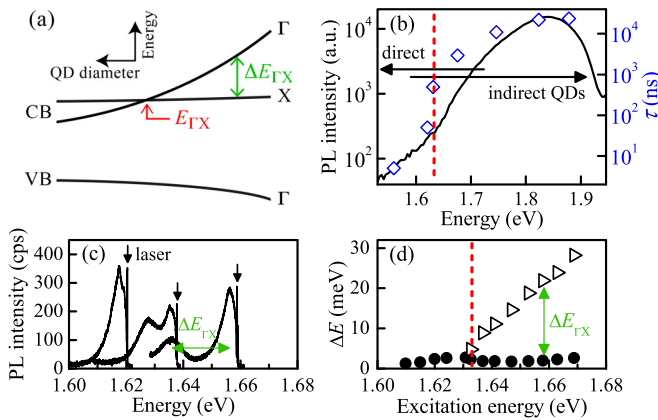


FIG. 1. (Color online) (a) Band alignment in (In,Al)As/AlAs QDs as a function of dot diameter for the valence (VB) and conduction (CB) bands. The energy difference between Γ - and X -electron states is denoted by $\Delta E_{\Gamma X}$. For a particular diameter, Γ - X crossover occurs, corresponding to a gap energy $E_{\Gamma X}$. (b) The PL spectrum of an (In,Al)As/AlAs QD ensemble at $T = 1.8$ K; excitation photon energy $E_{\text{exc}} = 2.33$ eV. The exciton recombination times τ across the ensemble are shown by open diamonds (right scale). (c) Resonantly excited PL of direct and indirect excitons around the Γ - X crossover. The laser photon energies are marked by arrows. (d) Difference between laser energy and the peak position of the direct (circles) and indirect (triangles) exciton PL.

corresponding crossing energy is marked in Fig. 1(a) by $E_{\Gamma X}$. Note that the quantum confinement and strain split the degenerate X -electron states into X_{xy} and X_z states with the valley main axis being perpendicular and parallel to the z axis, respectively. The X_{xy} state has lower energy [17], and we refer to it as the X -valley electron state in the following.

The coexistence of QDs with mainly direct and indirect band gaps within the ensemble is evidenced by the spectral dependence of the radiative exciton recombination times τ . As shown in Fig. 1(b), the indirect QDs are characterized by long decay times in the μs range due to the small exciton oscillator strength [12]. On the contrary, in the direct band gap dots, the excitons recombine within a few nanoseconds. In the Γ - X -crossover range, the X -valley conduction-band component in the exciton wave function gradually increases, thus making the exciton more indirect and extending its lifetime. The crossing energy of the Γ and X levels is spread over the 1.6–1.7 eV energy range due to QD parameter variations.

Further insight into the Γ - X crossing can be obtained from photoluminescence (PL) under resonant excitation, which selects only a fraction of dots in the ensemble, causing line narrowing due to reduced inhomogeneous broadening. One can see in Fig. 1(c) that for low-energy excitation with $E_{\text{exc}} < E_{\Gamma X}$, only the largest dots hosting direct excitons are excited, thus resulting in a spectrally narrow PL line. For excitation energies exceeding $E_{\Gamma X}$, an additional broad PL line appears, which originates from indirect exciton emission. The separation ΔE of the emission line maximum from the varying laser photon energy is plotted in Fig. 1(d). The direct excitons (circles) closely follow E_{exc} with a small shift $\Delta E = (2.2 \pm 0.1) \text{ meV}$. This shift arises from excitation through an acoustic phonon, which is most efficient for the phonon wavelength matching the dot size. On the other hand, the shift of the indirect exciton PL line (triangles) increases markedly and linearly with E_{exc} , as the recombination energy remains almost fixed. The meeting point of both shifts at 1.633 eV occurs at $E_{\Gamma X}$, indicated by the dashed line.

III. SPIN-LEVEL STRUCTURE OF INDIRECT EXCITON

Now, let us determine the exciton spin-level structure by SFRS. Raman spectra recorded at magnetic fields of 4 and 5 T in a tilted geometry ($\theta = 75^\circ$), essential for the symmetry breaking required for spin flips, are shown in Fig. 2(a) for excitation at the Γ - X -crossover energy. Three SFRS lines corresponding to the heavy hole, X -valley electron and indirect exciton (Ex) are observed in the Stokes and anti-Stokes regions. Their spin-flip Raman shifts ΔE_{SF} correspond to transitions between Zeeman sublevels split by $|g|\mu_B B$ with the Bohr magneton μ_B . The magnetic field dependences of the Raman shifts are depicted in Fig. 2(b). Lines represent linear fits yielding g factors of $|g_e^\theta| = 2.00 \pm 0.01$, $|g_{\text{Ex}}^\theta| = 1.24 \pm 0.02$, and $|g_{\text{hh}}^\theta| = 0.75 \pm 0.01$ for $\theta = 75^\circ$. Note that the full width at half maximum taken from the Gaussian fit of the hh-SFRS line is about 20% larger than that for the electron, which indicates a broader heavy-hole g -factor dispersion.

The angular dependence of the g factors at $B = 5$ T is demonstrated in Fig. 3(a). The shift of the e-SFRS line is isotropic, $g_e \equiv g_e^\parallel = g_e^\perp$, with $g_e = 2.00 \pm 0.01$. The g -factor isotropy and magnitude are characteristic for X -valley

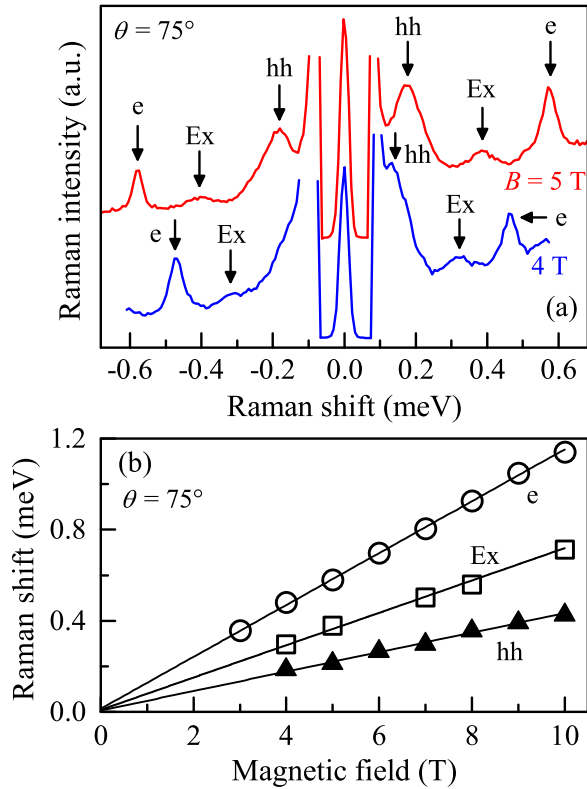


FIG. 2. (Color online) (a) Stokes and anti-Stokes SFRS spectra for magnetic fields of 4 and 5 T in tilted geometry with crossed linear polarization. Resonant excitation close to the Γ -X crossing at 1.636 eV. (b) Dependences of Raman shifts on the magnetic field; lines are linear fits.

electrons in indirect band gap structures [19,20]. Due to the large band gap at the X point (≈ 4.8 eV between conduction and valence band), the spin-orbit contribution to the electron g factor is vanishingly small [21]. As a result, the measured value coincides with the free-electron Landé factor.

The angular-dependent g factors in Fig. 3(a) are assigned to the heavy hole and indirect exciton. The hh g factor for a particular field direction is determined by its tensor components along and normal to the growth direction through $g_{hh}(\theta) = [(g_{hh}^{\parallel} \cos \theta)^2 + (g_{hh}^{\perp} \sin \theta)^2]^{1/2}$. As seen from the corresponding fit (dashed line), $g_{hh}(\theta)$ describes well the experimental data with $g_{hh}^{\parallel} = 2.42 \pm 0.05$ and $g_{hh}^{\perp} = 0.03 \pm 0.05$. The small transverse hh g factor indicates a weak mixing of the light hole (lh) and heavy hole at the Γ point compared to, e.g., (In,Ga)As/GaAs QDs [22].

Bearing in mind the isotropy of g_e and the positive sign of g_{hh}^{\parallel} , we can evaluate the indirect exciton g factor from $g_{Ex}(\theta) = g_{hh}(\theta) - g_e$. The calculated dependence for $g_{Ex}(\theta)$ shown by the solid line in Fig. 3(a) is in good accord with the data. The following exciton g -factor values are obtained: $g_{Ex}^{\parallel} = 0.43 \pm 0.08$ and $g_{Ex}^{\perp} = -1.95 \pm 0.08$. The positive sign of g_{Ex}^{\parallel} is supported by the magnetic-field-induced circular polarization of the QD photoluminescence measured in Faraday geometry. The circular polarization degree defined as $\rho_c = (I^+ - I^-)/(I^+ + I^-)$ is evaluated from the intensities I^+ and I^- of the σ^+ and σ^- polarized exciton emission,

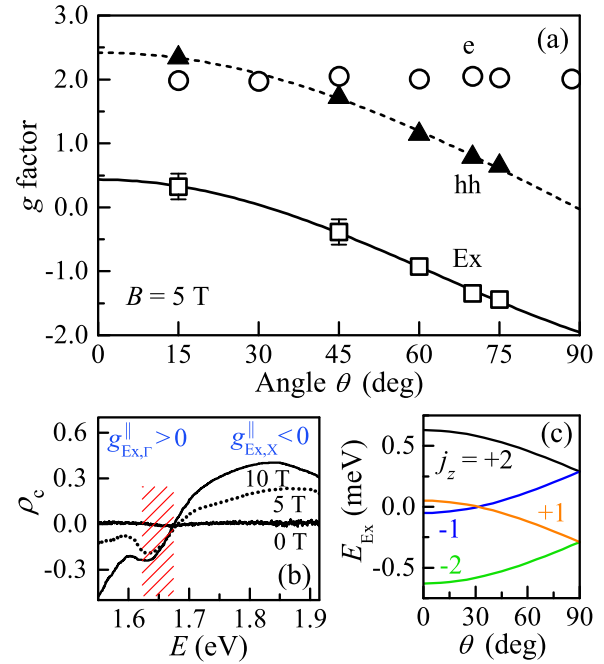


FIG. 3. (Color online) (a) g -factor angle dependence for heavy hole, X-valley electron and indirect exciton. Dashed line is the fit for $g_{hh}(\theta)$, solid line is the calculation for $g_{Ex}(\theta)$; see text. Note that the points $g_{Ex}(15^\circ)$ and $g_{Ex}(45^\circ)$ are evaluated from the measured e and hh g factors. (b) Magnetic-field-induced circular polarization degree of the QD photoluminescence measured in Faraday geometry at different magnetic fields and a laser power of 1 mW/cm²; $E_{Ex} = 2.33$ eV, $T = 1.8$ K. (c) Calculated energies of angle-dependent bright and dark exciton states at the Γ -X-crossing point, $B = 5$ T. The center of gravity is taken as zero.

respectively. A negative ρ_c , given for $I^- > I^+$, means that the exciton state $| -1 \rangle$ is lower in energy than that of the $j_z = +1$ exciton and, in turn, the longitudinal exciton g factor is positive.

The spectral dependence of ρ_c measured for the studied (In,Al)As/AlAs QDs at three different magnetic fields is shown in Fig. 3(b). One can see that the polarization degree is vanishingly small at zero magnetic field and increases with growing field strength. It changes its sign across the emission band of the ensemble consisting of direct and indirect band gap QDs. In the case of direct QDs at low energies (< 1.62 eV), ρ_c is negative, which evidences that the g factor of the direct excitons is positive, $g_{Ex,\Gamma}^{\parallel} > 0$.

In the spectral range of indirect band gap QDs (> 1.67 eV), ρ_c becomes positive. Here, the longitudinal g factor of the indirect exciton is negative, $g_{Ex,X}^{\parallel} < 0$. Due to the isotropic X-valley electron g factor, $g_e^{\parallel} = g_e = 2.00$, the relation $|g_{hh}^{\parallel}| < |g_e|$ is valid for $E > 1.67$ eV. Keeping in mind that at 1.636 eV, $|g_{hh}^{\parallel}| = 2.42$, we conjecture that the heavy-hole g factor decreases with increasing band gap energy.

In the Γ -X-crossing region, marked by the dashed area in Fig. 3(b), ρ_c is provided by the emission of the mixed excitons. The polarization degree in this region changes with increasing energy from the negative values, being characteristic for the direct excitons, to the positive values of the indirect excitons.

At the energy of 1.636 eV, $\rho_c < 0$, which corresponds to a positive g factor and is in agreement with the SFRS results measured in the Γ - X -mixing regime.

In the following, the exciton fine structure will be calculated as a function of the tilt angle. Assuming a tilted geometry with $\theta \neq 0^\circ$, the in-plane component $B_x = B \sin \theta$ of the magnetic field $\mathbf{B} = B(\sin \theta, 0, \cos \theta)$ induces a mixing of the electron spin basis eigenstates. Since the light-hole and heavy-hole states at the Γ point are not mixed and QD shape anisotropies are negligible, the symmetry of the QDs is, to a good approximation, D_{2d} . The corresponding magnetic-field-dependent Hamiltonian takes the form

$$\hat{H}_B = \frac{1}{2}\mu_B(g_e^\parallel \cos \theta \sigma_z B_z + g_e^\perp \sin \theta \sigma_x B_x) + g_0\mu_B(\kappa_{KL}j_{z,hh}B_z + q_{KL}j_{z,hh}^3 B_z). \quad (1)$$

Here, g_0 is the free-electron g factor, $\sigma_{x,z}$ are Pauli matrices, and $j_{z,hh}$ is the z component of the hh angular momentum operator. The non-Zeeman term of the heavy hole has the symmetry of the Kohn-Luttinger Hamiltonian [23,24]. κ_{KL} and q_{KL} are the Kohn-Luttinger parameters. Only the second electron Zeeman term introduces an off-diagonal coupling between the electron spin basis eigenstates $|+1/2\rangle = |\uparrow\rangle$ and $|-1/2\rangle = |\downarrow\rangle$. The spin states are then superpositions of the type $|\Psi_e^\pm\rangle = \alpha|\pm 1/2\rangle \pm \beta|\mp 1/2\rangle$ with the mixing coefficients $\alpha = \cos(\theta/2)$ and $\beta = \sin(\theta/2)$. These spin states are used to describe both the Γ - and X -valley electron. The heavy-hole spin states are given by $|\Psi_{hh}^+\rangle = |+3/2\rangle = |\uparrow\rangle$ and $|\Psi_{hh}^-\rangle = |-3/2\rangle = |\downarrow\rangle$. The confined exciton states can be factorized into the product of the heavy-hole and electron ones: $|\Psi_{Ex}^{\pm,\pm}\rangle = |\Psi_{hh}^\pm\rangle \cdot |\Psi_e^\pm\rangle$. As an example, the $|\Psi_{Ex}^{+,-}\rangle$ exciton consists of a $j_{z,hh} = +3/2$ heavy hole and an electron in the state $|\Psi_e^-\rangle$.

The energies of the indirect exciton, which are calculated on the basis of Eq. (1), are plotted in Fig. 3(c). They are given by

$$E_{Ex}^{+,+} = -E_{Ex}^{-,-} = \frac{1}{2}\mu_B B(g_e + g_{hh}^*), \quad (2)$$

$$E_{Ex}^{+,-} = -E_{Ex}^{-,+} = \frac{1}{2}\mu_B B(g_e - g_{hh}^*), \quad (3)$$

with $g_{hh}^* = 3g_0 \cos \theta(\kappa_{KL} + \frac{9}{4}q_{KL})$. An isotropic electron g factor of $g_e = 2$ is used, and the Kohn-Luttinger parameters are estimated [25] to $\kappa_{KL} = 0.317$ and $q_{KL} = 0.033$. The angular dependence demonstrates a crossing of the exciton states $|\Psi_{Ex}^{+,-}\rangle$ and $|\Psi_{Ex}^{-,+}\rangle$ at an angle of about 30° . Here, the exciton-SFRS shift vanishes. Also, at this crossing angle, the exciton g factor changes its sign. In the Voigt geometry, the dark and bright exciton states are fully mixed. As evaluated from the simulated dependence $E_{Ex}(\theta)$, all three SFRS lines should be observable at $\theta \approx 75^\circ$, which is confirmed experimentally by the observation of the three SFRS processes; see Fig. 2(a).

IV. MECHANISMS AND EFFICIENCIES OF SPIN-FLIP RAMAN SCATTERING PROCESSES

Now, we study the mechanisms and efficiencies of the spin-flip processes induced by the resonant Raman scattering. As depicted in Fig. 4 for a close-to-Faraday geometry with $\theta = 15^\circ$ [27], the hh-SFRS is observed for crossed circular

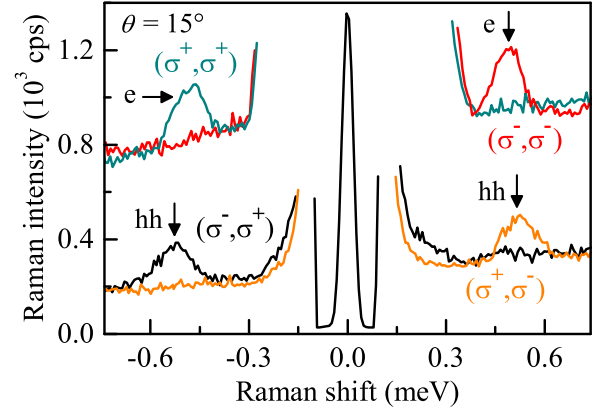


FIG. 4. (Color online) Cross-circularly and cocircularly polarized SFRS spectra measured at $B = 4$ T and $E_{exc} = 1.644$ eV.

polarizations in Stokes and anti-Stokes regions, while the e-SFRS line, having a smaller Raman shift, is present in copolarized configurations. These polarization properties of the SFRS lines define the optical selection rules. Considering the low-energetic (Stokes) electron spin-flip exemplarily (see Fig. 5), σ^- polarized light prepares the exciton in the state $|\downarrow\rangle(\alpha|\uparrow\rangle + \beta|\downarrow\rangle)$ with $\alpha > \beta$. An acoustic phonon with energy $\hbar\omega_{ph} = g_e\mu_B B$ reverses the electron spin state; hence, the intermediate scattering state is the indirect exciton $|\downarrow\rangle(\alpha|\downarrow\rangle - \beta|\uparrow\rangle)$. The Γ - X -valley mixing and particularly the mixed electron spin state in the tilted geometry enable the final exciton recombination yielding σ^- polarized light. The resonant SFRS is able to initialize spins, and by using incident light with opposite circular polarization, we can controllably switch from the electron to the hh spin-flip process, which is also mediated by an acoustic phonon. The efficiency of the SFRS-based manipulation of the electron and hole spins for the excitation at the Γ - X -crossing point can be evaluated to about 20% from comparison with the quantum yield of the resonant

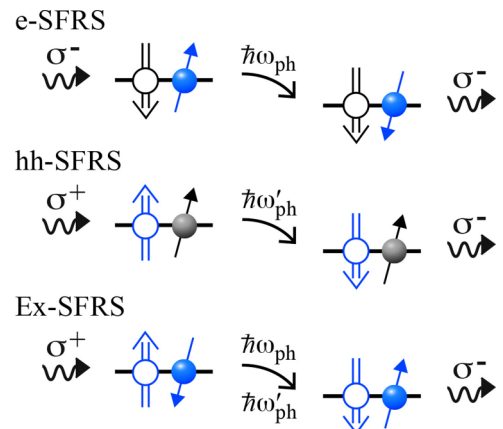


FIG. 5. (Color online) Schemes of the SFRS Stokes processes. The curved lines represent the incident and outgoing light, the tilted arrows indicate the mixed electron spin states, and the carriers participating in the spin-flip processes are shown in blue. Acoustic phonon energy $\hbar\omega_{ph}$ is equal to $g_{hh}\mu_B B$.

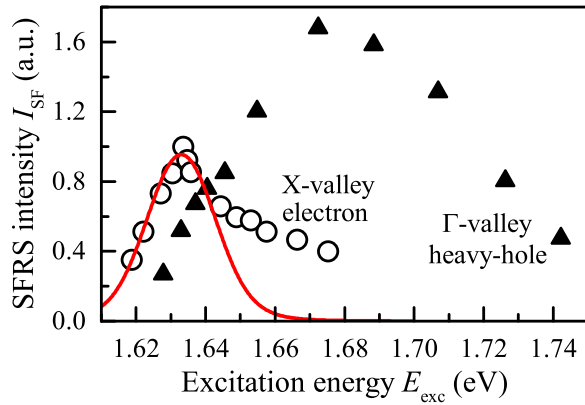


FIG. 6. (Color online) The e- and hh-SFRS resonance profiles as measure of the spin-flip scattering efficiencies; $B = 5$ T, $T = 1.8$ K, $\theta = 75^\circ$. The red curve represents the theoretically modeled e-SFRS efficiency based on Eq. (9).

PL [28]. It strongly depends on QD ensemble parameters and the degree of Γ -X mixing, as will be discussed below.

The exciton spin flip involves both bright exciton states and requires simultaneous reversals of the electron and hole spins, as demonstrated in Fig. 5, either due to one-phonon or two-phonon processes [29,30]. In the one-phonon process, the simultaneous flip would occur via the heavy- and light-hole-exciton mixing owing to the interplay of exchange interactions and lattice deformations. The two-phonon exciton spin flip is a double-quantum transition with a virtual intermediate state, which does not require exchange interaction. Hence, the spin of the indirect exciton is very likely flipped by the two-phonon process, while the one-phonon process is less probable due to the weak hh-lh mixing. Note that in contrast to direct-gap semiconductors where the exchange constants are contributed by both short- and long-range exchange interactions [31,32], for the long-lived indirect excitons only the short-range exchange interaction is important. The one-phonon process would then be mediated by the short-range exchange interaction.

The intensities of the e- and hh-SFRS lines that characterize the efficiencies of the Raman scattering processes are plotted in Fig. 6 as the laser photon energy E_{exc} is tuned across the QD ensemble. The spectral profile of the hh-SFRS intensity is much broader than that for the electron, and has a maximum at about 1.680 eV. However, its width is narrower than that of the ensemble PL spectrum. The profile can be explained by Raman scattering involving the direct exciton state. The spectral density of QDs shapes the low-energy side of the profile. The decrease at the high-energy side is due to shortening of the direct exciton lifetime caused by electron scattering from the Γ to the X valley. This process becomes efficient when the energy of the Γ valley exceeds that of the X valley by the longitudinal-optical phonon energy, which is 30 meV for InAs and 49 meV for AlAs phonons [33].

The X-valley electron SFRS intensity, shown by the open circles, has a sharp maximum at $E_{\text{max}} = 1.633$ eV, which is the crossing energy $E_{\Gamma X}$ of the Γ - and X-electron valleys. Qualitatively, this can be understood by taking into account that one-photon excitation of a pure indirect exciton is

forbidden, but can be achieved by mixing the direct exciton with the indirect one. This admixture is provided by mixing of the Γ and X electrons. The X-valley electron SFRS intensity is expected to be maximum when the Γ and X valleys are in resonance.

For an in-depth understanding of the SFRS process involving the Γ -X mixed exciton states, we propose a model to calculate the efficiency of the e-SFRS process and its Raman spectrum. We consider the QDs as an ensemble of two-level systems with wave function

$$\Psi = C_\Gamma |\Gamma\rangle + C_X |X\rangle. \quad (4)$$

Here, the coefficients carry information about the ensemble (described later), and $|q\rangle$ ($q = \Gamma, X$) are two orthonormalized basis states in an individual two-level quantum system characterized by the unperturbed eigenenergies E_q . In the regime of Γ -X mixed states, we consider a low-lying level with the energy

$$E^- = \frac{E_\Gamma + E_X}{2} - \frac{1}{2} \sqrt{(E_\Gamma - E_X)^2 + 4V_{\Gamma X}^2},$$

where the coefficients C_q^- are given by

$$|C_\Gamma^-|^2 = \frac{1}{2} \left(1 - \frac{\Delta}{\sqrt{\Delta^2 + \delta^2}} \right),$$

$$|C_X^-|^2 = \frac{1}{2} \left(1 + \frac{\Delta}{\sqrt{\Delta^2 + \delta^2}} \right).$$

Here, $\Delta \equiv \Delta_{E_{\Gamma X}} = E_\Gamma - E_X$, and $\delta = 2|V_{\Gamma X}|$ is the modulus of the matrix element of the coupling between the states $|\Gamma\rangle$ and $|X\rangle$ due to their mixing in an individual quantum system. For the high-lying level with the energy

$$E^+ = \frac{E_\Gamma + E_X}{2} + \frac{1}{2} \sqrt{(E_\Gamma - E_X)^2 + 4V_{\Gamma X}^2},$$

the coefficients C_q^+ read

$$|C_\Gamma^+|^2 = \frac{1}{2} \left(1 + \frac{\Delta}{\sqrt{\Delta^2 + \delta^2}} \right),$$

$$|C_X^+|^2 = \frac{1}{2} \left(1 - \frac{\Delta}{\sqrt{\Delta^2 + \delta^2}} \right).$$

The g factor of this two-level quantum system is defined by

$$g^\pm \equiv g(\Delta) = g_\Gamma |C_\Gamma^\pm|^2 + g_X |C_X^\pm|^2, \quad (5)$$

where g_Γ and g_X are the single-valley g factors. The absence of a further e line in the SFRS spectrum of Fig. 2(a) suggests that the value of g_Γ in the studied dot structures is small and hereafter we set it equal to zero for simplicity. One could account in the theoretical model for a small but finite g_Γ value. It would not significantly change the calculation results presented here, however, the equations would become rather bulky. In the following, among the two split states, we only consider the one with $|C_X| > |C_\Gamma|$ because the other state does not contribute notably to the e-SFRS line in Figs. 2(a) and 4.

For a resonant three-step process, including (i) photon absorption expressed by the incident photon energy $\hbar\omega_i = E_{\text{exc}}$, (ii) acoustic phonon-induced spin flip, and (iii) emission of a secondary photon with energy $\hbar\omega_f$, the scattering intensity

takes the form

$$I_{sc} \propto I_i W_{em} \tau_{l\bar{j}} W_{sf} \tau_{lj} W_{abs}. \quad (6)$$

Here, I_i is the intensity of the incident light, j is the exciton spin with $\bar{j} = -j$, and τ_{lj} is the lifetime of the exciton in the state $|lj\rangle$ with $l = \pm$ as the index of the split levels. The probability rates for the absorption, emission, and spin flip are proportional to

$$\begin{aligned} W_{abs} &\propto |M_{lj,0}(\mathbf{e}_i)|^2 \delta(E_{lj} - \hbar\omega_i), \\ W_{em} &\propto |M_{0,l\bar{j}}(\mathbf{e}_f^*)|^2 \delta(E_{l\bar{j}} - \hbar\omega_f), \\ W_{sf} &\propto \sum_{k_{ph}} |V_{l\bar{j},lj}|^2 \left(N_{ph} + \frac{1 \mp 1}{2} \right) \delta(E_{l\bar{j}} - E_{lj} \pm \hbar v_{ph} k_{ph}). \end{aligned} \quad (7)$$

The matrix elements of the involved processes are described by $V_{l\bar{j},lj}$, $M_{lj,0}(\mathbf{e}_i)$, and $M_{0,l\bar{j}}(\mathbf{e}_f^*)$, where the last two include the ground state $|0\rangle$ of the crystal. The polarization unit vectors are designated by \mathbf{e}_i and \mathbf{e}_f . N_{ph} is the phonon occupation number, v_{ph} is the sound velocity, and k_{ph} is the wave number of the acoustic phonon. The signs in Eq. (7) account for Stokes (-) and anti-Stokes (+) processes. According to Ref. [34], the probability rate of the acoustic-phonon-assisted electron spin flip is proportional to $(E_{l\bar{j}} - E_{lj})^N$ with $N \approx 3-5$, so that $W_{sf} \propto [|C_X|^2]^N$. The exciton lifetime τ_{lj} is contributed by the nonradiative lifetime τ_{nr} and radiative lifetime τ_r of the Γ -valley exciton,

$$\frac{1}{\tau_{lj}} = \frac{|C_\Gamma|^2}{\tau_r} + \frac{1}{\tau_{nr}} \quad \Leftrightarrow \quad \tau_{lj} = \frac{\tau_r}{|C_\Gamma|^2 + \frac{\tau_r}{\tau_{nr}}}.$$

For resonant excitation, the exciton recombination via nonradiative channels is assumed to be slow: $\tau_{nr} \gg \tau_r$.

Now, we express the ensemble character of the modeled quantum system with its different dot sizes and shapes via a dispersive Γ - X -level splitting D . This shall be given by the sum of the average value $\tilde{\Delta}$ (dependent on the excitation energy E_{exc} or, respectively, incident frequency ω_i) and the random value $\tilde{\Delta}$. The distribution of $\tilde{\Delta}$ is assumed to be described by a Gaussian function with width Δ_0 :

$$F(\tilde{\Delta}) = \frac{1}{\sqrt{\pi} \Delta_0} \exp\left(-\frac{\tilde{\Delta}^2}{\Delta_0^2}\right). \quad (8)$$

The dispersion of $\tilde{\Delta}$ shall exceed δ and the Zeeman splitting $g_e \mu_B B = E_{q,1/2} - E_{q,-1/2}$. Then one obtains for the spin-flip Raman scattering intensity $I_{SF}(E_{exc}) := I_{sc}(\omega_i)$,

$$\begin{aligned} I_{SF}(E_{exc}) &\propto \int_{-\infty}^{\infty} d\tilde{\Delta} F(\tilde{\Delta}) \left[\frac{\sqrt{D^2 + \delta^2} - D}{(1 + 2\alpha)\sqrt{D^2 + \delta^2} - D} \right]^2 \\ &\times \left(1 + \frac{D}{\sqrt{D^2 + \delta^2}} \right)^N, \end{aligned} \quad (9)$$

with $D = |\tilde{\Delta}(E_{exc}) + \tilde{\Delta}|$ and $\alpha = \tau_r/\tau_{nr}$. For simplicity, it is assumed that δ and Δ_0 are independent of E_{exc} . For the average splitting $\tilde{\Delta}$, we postulate a linear dependence,

$$\tilde{\Delta}(E_{exc}) = \eta(E_{exc} - E_{max}),$$

where E_{max} is the energy of the incident light at which the photoexcited Γ and X levels merge on average. The parameter η is estimated to 0.65 from the slope of the dependence given by the triangles in Fig. 1(d). Note that for $\delta/\Delta_0, \tau_r/\tau_{nr} \ll 1$, the scattering intensity I_{SF} is insensitive to the integer power N in Eq. (9).

Equation (9) describes well the experimental e-SFRS intensity data, as shown by the red curve for $N = 5$ in Fig. 6. From the simulation, we obtain accurate values for the involved parameters, in particular $\delta = 0.8$ meV, and also $\Delta_0 = 10$ meV as well as $\alpha \leq 10^{-2}$. The high-energy tail observed in the resonance profile is caused by a more complex distribution of QD sizes than the assumed Gaussian. Nevertheless, Eq. (9) provides a reliable way to estimate the strength of the Γ - X coupling by $V_{\Gamma X} = \delta/2 = 0.4$ meV for the studied QD ensemble.

In order to calculate the SFRS spectrum, one should perform the integration in Eq. (9) with the δ function of the form $\delta(\Omega - |C_X(\tilde{\Delta})|^2)$. The dimensionless frequency Ω is given by $\frac{\hbar(\omega_i - \omega_f)}{g_x \mu_B B}$. Here, the difference between the incident and final photon energies is normalized to the Zeeman splitting of the pure X state. Ω can vary between zero for the pure Γ state (by assuming $g_r = 0$ for simplicity) and unity for the pure X state; $\Omega = 1$ corresponds to $g_x = 2$. The expressions for $|C_X|^2$ and $|C_\Gamma|^2$ are then replaced by the following ones:

$$\begin{aligned} |C_X|^2 &= 1 + \frac{|\Delta|}{\sqrt{\Delta^2 + \delta^2}} = \Omega, \\ |C_\Gamma|^2 &= 1 - |C_X|^2 = 1 - \Omega. \end{aligned}$$

The integration of the δ function results in the following density of states:

$$\rho(\Omega) \propto \frac{1}{[1 - (2\Omega - 1)^2]^{3/2}}.$$

Finally, one obtains for the SFRS spectrum ($N = 5$),

$$\begin{aligned} I_{SF}(\Omega) &\propto \frac{e^{-\Delta_+^2/\Delta_0^2} + e^{-\Delta_-^2/\Delta_0^2}}{\sqrt{\pi} \Delta_0} \left(\frac{\Omega - 1}{\Omega - 1 + \alpha} \right)^2 \\ &\times \frac{\Omega^5}{[1 - (2\Omega - 1)^2]^{3/2}} \\ &= \frac{e^{-\Delta_+^2/\Delta_0^2} + e^{-\Delta_-^2/\Delta_0^2}}{8\sqrt{\pi} \Delta_0} \frac{\Omega^{7/2} \sqrt{1 - \Omega}}{(1 + \alpha - \Omega)^2}. \end{aligned} \quad (10)$$

Here, the energy splittings Δ_{\pm} take the form

$$\Delta_{\pm} = -\tilde{\Delta}(E_{exc}) \pm \frac{\delta|2\Omega - 1|}{2\sqrt{\Omega(1 - \Omega)}}. \quad (11)$$

A simulated Raman spectrum for $E_{exc} = 1.636$ eV and $\delta = 0.8$ meV is presented in Fig. 7(a). Only the X valley contributes to that Raman spectrum by a sharp line. The model adequately describes the Raman shift of the e-SFRS line. The analysis demonstrates that for $\alpha \ll 1$, the effective dispersion of the g factor, leading to the inhomogeneous Raman linewidth, is much smaller than that of the experimental line, which is mainly determined by the spectral width of the monochromator slits. For very weakly coupled Γ and X states with $\delta = 0.008$ meV, one obtains two sharp Raman peaks at $g_r \approx 0.2$ (g_r set to > 0) and $g_x = 2$; see Fig. 7(b).

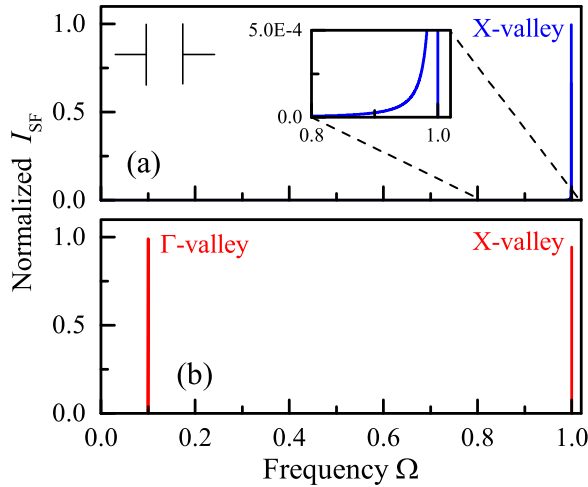


FIG. 7. (Color online) (a) Simulated Raman spectrum for an X -valley state, after Eq. (10), and scheme of the spectral bandpass of the monochromator slits. Inset: The smooth tail of the X -valley line for $\Omega < 1$. (b) Simulated Raman spectrum for Γ - and X -valley states in the case of very weak Γ - X coupling ($\delta = 0.008$ meV).

The theoretical approach provides reliable numerical data for simulating the Raman line of both the Γ as well as the X level in the Γ - X -crossing region. The approximations for the SFRS intensities $I_{\text{SF}}(E_{\text{exc}})$ and $I_{\text{SF}}(\Omega)$ and comparisons with the exact solutions can be found in the Appendix.

In ideal bulk semiconductors, the electron states from the Γ and X valleys do not mix with each other; however, Γ - X mixing does take place in low-dimensional heterostructures due to reflection of the electron from the interfaces. For (001)-oriented GaAs/AlAs superlattices with type-II band alignment, where strain and quantum confinement lift the level degeneracy at the X valley of the AlAs layer [35,36], considerable Γ - X_z mixing is provided by the uncertainty of the electron k vector, k_z , perpendicular to the interface [37]. The Γ - X_{xy} mixing can be induced only by violation of the translational symmetry in the xy plane, which is absent in superlattices with flat interfaces. However, this violation is possible in QDs due to their boundaries perpendicular to the (001) direction. For the (In,Al)As/AlAs QDs, this mechanism is responsible for the strong variation of the exciton recombination rate that is affected by the annealing treatment during growth [12], which in turn changes the Γ - X_{xy} mixing. SFRS is therefore able to characterize the Γ - X_{xy} mixing quantitatively, opening up an alternative way for systematic studies of intervalley coupling and spin-flip scattering processes in semiconductors.

V. CONCLUSION

To conclude, we have shown that the spin-level structure and spin-flip mechanism of the exciton that is indirect in momentum space in type-I (In,Al)As/AlAs QDs can be assessed by resonant spin-flip Raman scattering due to its mixing with the optically allowed direct exciton. The SFRS itself is a coherent manipulation, as it can be used to initialize and orient the spins of the electron, the heavy hole, and, in particular, the exciton. This tool can also be applied to other indirect systems with, e.g., Γ -L-valley mixed excitons

or type-II band alignment. Moreover, our study implies that it is worthwhile to further attempt tailoring of the band structure of such mixed direct-indirect systems, as in that way one can obtain long-lived excitons with appealing spin properties that do not only have long relaxation times but can also be manipulated by optical or electrical methods. These QD structures are promising for quantum information technologies.

ACKNOWLEDGMENTS

This work was supported by the Deutsche Forschungsgemeinschaft via SPP 1285, Mercator Research Center Ruhr (MERCUR) of Stiftung Mercator, Russian Foundation for Basic Research (Grants No. 13-02-00073 and No. 14-02-00033), Russian Ministry of Education and Science (Contract No. 11.G34.31.0067), and Russian Federation President Grant No. NSH-1085.2014.2. V.F.S. and M.B. acknowledge partial financial support from the Russian Ministry of Education and Science (Contract No. 14.Z50.31.0021).

APPENDIX: TRANSFORMATIONS AND APPROXIMATIONS OF EQUATIONS FOR SFRS INTENSITIES

In the following, we derive approximations for the SFRS intensities $I_{\text{SF}}(E_{\text{exc}})$ and $I_{\text{SF}}(\Omega)$, and compare them with the exact solutions.

1. SFRS resonance profile, $I_{\text{SF}}(E_{\text{exc}})$

Let us pay attention to Eq. (9) assuming α to be very small. We multiply this equation by

$$S = \frac{\sqrt{D^2 + \delta^2} + D}{(1 + 2\alpha)\sqrt{D^2 + \delta^2} + D},$$

and divide by the same S . Then we can reduce the ratio,

$$\frac{\sqrt{D^2 + \delta^2} - D}{(1 + 2\alpha)\sqrt{D^2 + \delta^2} - D},$$

to

$$\frac{(\sqrt{D^2 + \delta^2} - D)(\sqrt{D^2 + \delta^2} + D)}{[(1 + 2\alpha)\sqrt{D^2 + \delta^2} - D][(1 + 2\alpha)\sqrt{D^2 + \delta^2} + D]} \times \frac{1}{S}.$$

For the first factor of the last expression, we can write the following approximation:

$$\begin{aligned} & \frac{(\sqrt{D^2 + \delta^2} - D)(\sqrt{D^2 + \delta^2} + D)}{[(1 + 2\alpha)\sqrt{D^2 + \delta^2} - D][(1 + 2\alpha)\sqrt{D^2 + \delta^2} + D]} \\ &= \frac{\delta^2}{[(1 + 2\alpha)^2 - 1]D^2 + (1 + 2\alpha)^2\delta^2} \\ &\approx \frac{\delta^2}{4\alpha D^2 + \delta^2}. \end{aligned}$$

For small α , we can replace S by unity and obtain

$$\frac{\sqrt{D^2 + \delta^2} - D}{(1 + 2\alpha)\sqrt{D^2 + \delta^2} - D} \approx \frac{\delta^2}{4\alpha D^2 + \delta^2}.$$

Accordingly, Eq. (9) can be written as

$$I_{\text{SF}}(E_{\text{exc}}) \propto \int_{-\infty}^{\infty} d\tilde{\Delta} F(\tilde{\Delta}) \left(\frac{\delta^2}{4\alpha D^2 + \delta^2} \right)^2 Z$$

$$= \frac{1}{\sqrt{\pi}} \left(\frac{\delta^2}{4\alpha \Delta_0^2} \right)^2 \int_{-\infty}^{\infty} dt \frac{e^{-t^2} Z}{[(t+u)^2 + (\delta^2/4\alpha \Delta_0^2)]^2},$$

where $u = \tilde{\Delta}(E_{\text{exc}})/\Delta_0 = \eta(E_{\text{exc}} - E_{\Gamma X})/\Delta_0$ and

$$Z = \left(1 + \frac{D}{\sqrt{D^2 + \delta^2}} \right)^N = \left[1 + \frac{|t+u|}{\sqrt{(t+u)^2 + (\delta/\Delta_0)^2}} \right]^N.$$

We see that the function, which has to be analyzed, reads

$$f_1(u) = \frac{1}{\sqrt{\pi}} \int_{-\infty}^{\infty} dt \frac{e^{-t^2} Z(t,u)}{[(t+u)^2 + p^2]^2}, \quad (\text{A1})$$

with

$$p^2 = \frac{\delta^2}{4\alpha \Delta_0^2} = \frac{1}{4} \frac{\tau_{\text{nr}}}{\tau_r} \frac{\delta^2}{\Delta_0^2}.$$

One can expect that Z is close to unity for $\Delta_0 \gg \delta$, hence the function f_1 reduces to

$$f_2(u) = \frac{1}{\sqrt{\pi}} \int_{-\infty}^{\infty} dt \frac{e^{-t^2}}{[(t+u)^2 + p^2]^2}. \quad (\text{A2})$$

Now, we derive a further approximation related to the integral of the previous equation. In what follows, we first consider $f_2(u)$ at $u = 0$ and extend it to an arbitrary u .

In order to calculate the value of

$$f_2(0) \equiv I_2(p) = \frac{1}{\sqrt{\pi}} \int_{-\infty}^{\infty} dt \frac{e^{-t^2}}{(t^2 + p^2)^2},$$

we introduce the integral

$$I_n(p) = \frac{1}{\sqrt{\pi}} \int_{-\infty}^{\infty} dt \frac{e^{-t^2}}{(t^2 + p^2)^n},$$

and remind the reader of the table integral (integral 3.466 in Ref. [38]),

$$\frac{1}{\sqrt{\pi}} \int_0^{\infty} dx \frac{e^{-x^2}}{x^2 + \beta^2} = \frac{\sqrt{\pi}}{2\beta} e^{\beta^2} [1 - \Phi(\beta)],$$

where

$$\Phi(\beta) = \frac{2}{\sqrt{\pi}} \int_0^{\beta} e^{-t^2} dt.$$

Thus, one obtains

$$f_2(0) = -\frac{1}{2p} \frac{dI_1(p)}{dp} = -\frac{1}{2p} \frac{d}{dp} \left\{ \frac{\sqrt{\pi}}{p} e^{p^2} [1 - \Phi(p)] \right\}$$

$$= \frac{\sqrt{\pi}}{2p} \left\{ \left(\frac{1}{p^2} - 2 \right) e^{p^2} [1 - \Phi(p)] + \frac{2}{\sqrt{\pi} p} \right\}.$$

In order to calculate f_2 for an arbitrary u , we use the integral

$$\frac{1}{\sqrt{\pi}} \int_{-\infty}^{\infty} dt \frac{e^{-t^2}}{(t+u)^2 + p^2} = \frac{\sqrt{\pi}}{p} \text{Re}[e^{(p+iu)^2} \text{erfc}(p+iu)],$$

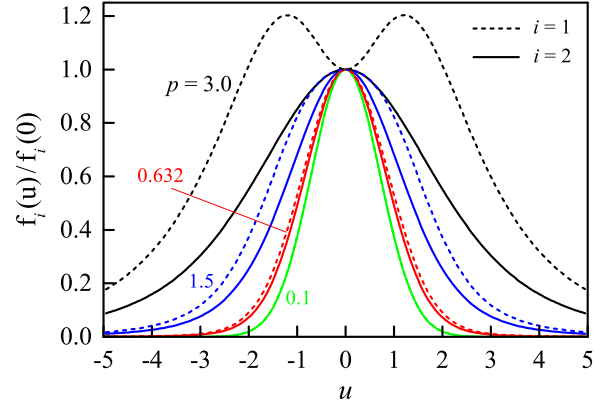


FIG. 8. (Color online) Simulated SFRS resonance profiles based on Eqs. (A1) and (A2) for different p values.

with $\text{erfc}(x) = 1 - \Phi(x)$. Then, it follows that

$$f_2(u) = \frac{\sqrt{\pi}}{2p} \text{Re} \left[\left(\frac{1 - 2ipu}{p^2} - 2 \right) e^{(p+iu)^2} \right. \\ \left. \times \text{erfc}(p+iu) + \frac{2}{\sqrt{\pi} p} \right]. \quad (\text{A3})$$

In Fig. 8, the numerical results of Eqs. (A1) and (A2), normalized to their values at $u = 0$ corresponding to the Γ - X -crossing point, are shown by the dashed and solid lines, respectively, for different values of the parameter p . Both functions provide similar data for $p < 2$, while for larger p values, f_1 shows two peaks being symmetrically positioned around $u = 0$. If we consider the parameters $\delta = 0.8$ meV, $\Delta_0 = 10$ meV, and $\alpha = 0.004$ determined as the ones describing the experimental results, then we obtain $p = 0.632$. In that case, both f_1 as well as f_2 , which is the approximation for $\Delta_0 \gg \delta$, are very similar, as depicted by the red lines. Note that the numerical data evaluated from Eq. (A3) fully coincide with that of Eq. (A2). We can conclude that the transformations and approximations derived from Eq. (9) are stable against changes in the parameters δ , Δ_0 , as well as α , and demonstrate reliable results in a broad energy range around the Γ - X -crossing point.

2. Raman spectrum, $I_{\text{SF}}(\Omega)$

We now analyze Eq. (10). By introducing the variable $\zeta = 1 - \Omega$, we have

$$I_{\text{SF}}(\zeta) \propto \frac{e^{-(\Delta_+/\Delta_0)^2} + e^{-(\Delta_-/\Delta_0)^2} (1-\zeta)^{7/2} \sqrt{\zeta}}{8\sqrt{\pi} \Delta_0 (\zeta + \alpha)^2}, \quad (\text{A4})$$

with the quantities

$$\frac{\Delta_{\pm}}{\Delta_0} = -u \pm \frac{v|1-2\zeta|}{2\sqrt{\zeta(1-\zeta)}}, \quad u = \frac{\tilde{\Delta}(E_{\text{exc}})}{\Delta_0}, \quad v = \frac{\delta}{\Delta_0}.$$

Assuming $\zeta \ll 1$, we can simplify this equation to

$$I_{\text{SF}}(\zeta) \propto e^{-u^2} e^{-v^2/(4\zeta)} \cosh \left(\frac{uv}{\sqrt{\zeta}} \right) \frac{\sqrt{\zeta}}{(\zeta + \alpha)^2}. \quad (\text{A5})$$

Here, the factor of proportionality is changed in comparison to Eq. (A4). For $\alpha \ll 1$, one can expect that the exact

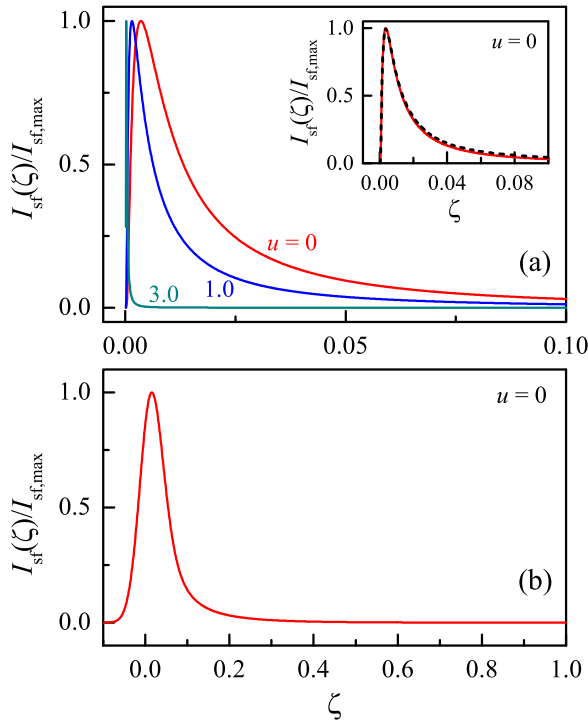


FIG. 9. (Color online) (a) Simulated SFRS spectra around $\zeta = 0$ for different u , after Eq. (A4). Inset: The simulations of Eq. (A4) (solid line) and Eq. (A5) (dashed line) for $u = 0$. (b) Raman line including spectral width of monochromator slits; Eq. (A4) convoluted with Gaussian function.

function (A4) and the approximation (A5) show a sharp peak at ζ close to 0 (or Ω close to 1).

In order to obtain a normalization for comparing different numerical results of $I_{\text{SF}}(\zeta)$, we derive in the following the maximum value $I_{\text{SF,max}}$. At $u = 0$, the Raman spectrum intensity (A5) reads

$$I_{\text{SF}}(\zeta; u = 0) \propto e^{-v^2/(4\zeta)} \frac{\sqrt{\zeta}}{(\zeta + \alpha)^2}.$$

The function $\sqrt{\zeta}/(\zeta + \alpha)^2$ reaches a maximum at $\zeta_m = \alpha/3$. The first derivative of $I_{\text{SF}}(\zeta; u = 0)$ is given by

$$\frac{e^{-v^2/(4\zeta)}}{2\sqrt{\zeta}} \left[\frac{\alpha - 3\zeta}{(\zeta + \alpha)^3} + \frac{v^2}{2\zeta^{3/2}} \right].$$

The position of maximum is found by setting the derivative to zero, which leads to the equation

$$\alpha - 3\zeta + \frac{v^2}{2\zeta^{3/2}}(\zeta + \alpha)^3 = 0,$$

or

$$\zeta = \frac{\alpha}{3} + \frac{v^2}{6\zeta^{3/2}}(\zeta + \alpha)^3.$$

By replacing ζ in the second term with the first-order approximation $\zeta_m^{(1)} = \alpha/3$, we find in the next-order approximation,

$$\zeta_m = \frac{\alpha}{3} + \frac{v^2}{6[\zeta_m^{(1)}]^{3/2}}[\zeta_m^{(1)} + \alpha]^3 = \frac{\alpha}{3} \left(1 + \frac{32}{3\sqrt{3}} v^2 \alpha^{1/2} \right).$$

We see that the correction is small when $v^2 \alpha^{1/2} \ll 1$, which is the case in our model. Starting from $\zeta = 0$, the function $I_{\text{SF}}(\zeta; u = 0)$ reaches the maximum at very small $\zeta = \zeta_m$ and then decreases with further increase in ζ .

Three curves $I_{\text{SF}}(\zeta)/I_{\text{SF,max}}$ for different u , evaluated from Eq. (A4), are shown in Fig. 9(a). The maximum of the Raman line shifts to $\zeta = 0$ with increasing u value, which corresponds to a decrease in Δ_0 . In comparison to the exact solution (A4), the approximation (A5) yields very similar results, as indicated exemplarily for $u = 0$ in the inset of Fig. 9(a). The steepness of the right flank of the Raman lines for small u corresponds well to that of the experimentally observed Raman lines; cf. Fig. 2(a). Moreover, in order to include the spectral width of the monochromator slits in the numerical considerations, we perform a convolution of the calculated spectrum with a Gaussian distribution $G(\zeta - \zeta')$, leading to $\int d\zeta' I_{\text{SF}}(\zeta') G(\zeta - \zeta')$. By use of the width 0.05 for the Gaussian function, we obtain for $u = 0$ the Raman line demonstrated in Fig. 9(b). Due to the implementation of the slit width, the intensity is larger than zero for $\zeta < 0$, and the shape is only slightly asymmetric: the simulation accords with the experiment.

To conclude, the transformed and approximated equations for both the SFRS resonance profile and the Raman spectrum in the Γ -X-mixing regime yield numerical results that are in good agreement with the experimental observations.

[1] E. U. Rafailov, M. A. Cataluna, and E. A. Avrutin, *Ultrafast Lasers Based on Quantum-dot Structures: Physics and Devices* (Wiley-VCH, Weinheim, 2011).
 [2] S. Cortez, O. Krebs, S. Laurent, M. Senes, X. Marie, P. Voisin, R. Ferreira, G. Bastard, J.-M. Gérard, and T. Amand, *Phys. Rev. Lett.* **89**, 207401 (2002).
 [3] C. Kammerer, C. Voisin, G. Cassabois, C. Delalande, Ph. Roussignol, F. Klopff, J. P. Reithmaier, A. Forchel, and J. M. Gérard, *Phys. Rev. B* **66**, 041306(R) (2002).
 [4] M. Kroutvar, Y. Ducommun, D. Heiss, M. Bichler, D. Schuh, G. Abstreiter, and J. J. Finley, *Nature (London)* **432**, 81 (2004).

[5] M. Sénès, B. Urbaszek, X. Marie, T. Amand, J. Tribollet, F. Bernardot, C. Testelin, M. Chamorro, and J.-M. Gérard, *Phys. Rev. B* **71**, 115334 (2005).
 [6] H. Yu, S. Lycett, C. Roberts, and R. Murray, *Appl. Phys. Lett.* **69**, 4087 (1996).
 [7] D. D. Awschalom and M. E. Flatté, *Nat. Phys.* **3**, 153 (2007).
 [8] J. Vučković and Y. Yamamoto, *Appl. Phys. Lett.* **82**, 2374 (2003).
 [9] A. Kress, F. Hofbauer, N. Reinelt, M. Kaniber, H. J. Krenner, R. Meyer, G. Böhm, and J. J. Finley, *Phys. Rev. B* **71**, 241304(R) (2005).

- [10] E. Poem, Y. Kodriano, C. Tradonsky, N. H. Lindner, B. D. Gerardot, P. M. Petroff, and D. Gershoni, *Nat. Phys.* **6**, 993 (2010).
- [11] T. S. Shamirzaev, A. V. Nenashev, A. K. Gutakovskii, A. K. Kalagin, K. S. Zhuravlev, M. Larsson, and P. O. Holtz, *Phys. Rev. B* **78**, 085323 (2008).
- [12] T. S. Shamirzaev, J. Debus, D. S. Abramkin, D. Dunker, D. R. Yakovlev, D. V. Dmitriev, A. K. Gutakovskii, L. S. Braginsky, K. S. Zhuravlev, and M. Bayer, *Phys. Rev. B* **84**, 155318 (2011).
- [13] A. V. Koudinov, Yu. G. Kusrayev, D. Wolverson, L. C. Smith, J. J. Davies, G. Karczewski, and T. Wojtowicz, *Phys. Rev. B* **79**, 241310(R) (2009).
- [14] J. Debus, D. Dunker, V. F. Sapega, D. R. Yakovlev, G. Karczewski, T. Wojtowicz, J. Kossut, and M. Bayer, *Phys. Rev. B* **87**, 205316 (2013).
- [15] A. A. Sirenko, V. I. Belitsky, T. Ruf, M. Cardona, A. I. Ekimov, and C. Trallero-Giner, *Phys. Rev. B* **58**, 2077 (1998).
- [16] J. Puls, M. Rabe, H.-J. Wünsche, and F. Henneberger, *Phys. Rev. B* **60**, R16303 (1999).
- [17] T. S. Shamirzaev, A. V. Nenashev, and K. S. Zhuravlev, *Appl. Phys. Lett.* **92**, 213101 (2008).
- [18] J.-W. Luo, A. Franceschetti, and A. Zunger, *Phys. Rev. B* **78**, 035306 (2008).
- [19] C. F. Young, E. H. Poindexter, G. J. Gerardi, W. L. Warren, and D. J. Keeble, *Phys. Rev. B* **55**, 16245 (1997).
- [20] E. E. Vdovin, Yu. N. Khanin, L. Eaves, M. Henini, and G. Hill, *Phys. Rev. B* **71**, 195320 (2005).
- [21] I. A. Yugova, A. Greilich, D. R. Yakovlev, A. A. Kiselev, M. Bayer, V. V. Petrov, Yu. K. Dolgikh, D. Reuter, and A. D. Wieck, *Phys. Rev. B* **75**, 245302 (2007).
- [22] I. A. Yugova, A. Greilich, E. A. Zhukov, D. R. Yakovlev, M. Bayer, D. Reuter, and A. D. Wieck, *Phys. Rev. B* **75**, 195325 (2007).
- [23] A. V. Koudinov, I. A. Akimov, Yu. G. Kusrayev, and F. Henneberger, *Phys. Rev. B* **70**, 241305(R) (2004).
- [24] Y. G. Semenov and S. M. Ryabchenko, *Phys. Rev. B* **68**, 045322 (2003).
- [25] The parameter q_{KL} is derived from the equation $xq_{\text{KL}}^{\text{InAs}} + (1-x)q_{\text{KL}}^{\text{AlAs}}$ with $x = 0.3$. The parameter κ_{KL} has been modified to simulate the experimental angle dependence of the SFRS. Thus, κ_{KL} used for the (In,Al)As QDs is about seven times smaller than the value 2.285 evaluated from bulk parameters [26].
- [26] I. Vurgaftman, J. R. Meyer, and L. R. Ram-Mohan, *J. Appl. Phys.* **89**, 5815 (2001).
- [27] We also performed Raman scattering experiments in the Faraday geometry and did not find any SFRS signal, as expected. Electron and heavy-hole spin flips are forbidden in the electric-dipole approximation for high potential symmetries [14]. On the other hand, the exciton spin flip is allowed in crossed circular polarizations, but cannot be resolved due to the rather small Zeeman splitting.
- [28] We estimate the average number of indirect excitons created within a QD subensemble by an incident laser beam with the spectral and spatial widths of $1 \mu\text{eV}$ and $250 \mu\text{m}$, and approximate their contribution to the SFRS signal with respect to the resonant PL.
- [29] V. F. Sapega, M. Cardona, K. Ploog, E. L. Ivchenko, and D. N. Mirlin, *Phys. Rev. B* **45**, 4320 (1992).
- [30] E. Tsitsishvili, R. v. Baltz, and H. Kalt, *Phys. Rev. B* **67**, 205330 (2003).
- [31] S. V. Gupalov and E. L. Ivchenko, *Phys. Solid State* **42**, 2030 (2000).
- [32] S. V. Goupalov and E. L. Ivchenko, *Phys. Solid State* **43**, 1867 (2001).
- [33] I. Ya. Karlik, D. N. Mirlin, and V. F. Sapega, *Sov. Phys. Semicond.* **21**, 630 (1987).
- [34] A. V. Khaetskii and Y. V. Nazarov, *Phys. Rev. B* **64**, 125316 (2001).
- [35] Y. Fu, M. Willander, E. L. Ivchenko, and A. A. Kiselev, *Phys. Rev. B* **47**, 13498 (1993).
- [36] V. Voliotis, R. Grousson, P. Lavallard, E. L. Ivchenko, A. A. Kiselev, and R. Planel, *Phys. Rev. B* **49**, 2576 (1994).
- [37] M.-H. Meynadier, R. E. Nahory, J. M. Worlock, M. C. Tamargo, J. L. de Miguel, and M. D. Sturge, *Phys. Rev. Lett.* **60**, 1338 (1988).
- [38] I. S. Gradshteyn and I. M. Ryzhik, *Table of Integrals, Series, and Products* (Academic Press, Burlington, 2007).